RSC Advances

PAPER

View Article Online
View Journal | View Issue



Cite this: *RSC Adv.*, 2018, **8**, 32948

# Novel high-efficiency $Eu^{3+}$-activated $Na_2Gd_2B_2O_7$ red-emitting phosphors with high color purity

Thangavel Sakthivel, Liangling Sun, Balaji Devakumar, Bin Li and Xiaoyong Huang *

In this study, a series of $Na_2(Gd_{1-x}Eu_x)_2B_2O_7$ (abbreviated as: $Na_2Gd_2B_2O_7$:$x$$Eu^{3+}$; $x$ = 0, 0.05, 0.15, 0.35, 0.45, and 0.50) phosphors were synthesized by conventional solid state reaction approach. The structure and morphology of the as-prepared phosphors were studied by X-ray diffraction, scanning electron microscopy and elemental mapping. The results indicated that the phosphors had micro-size particles with monoclinic phases. The photoluminescence excitation and emission study indicated that the as-prepared phosphors could give rise to efficient red emissions under near-ultraviolet excitation. The optimal doping concentration of $Eu^{3+}$ ions was $x$ = 0.35, and the corresponding deduced critical distance ($R_c$) was about 9.4 Å. The concentration quenching mechanism was dominated by energy-transfer among the $Eu^{3+}$ ions through dipole–dipole interactions. The calculated internal quantum efficiency of the $Na_2Gd_2B_2O_7$:0.35$Eu^{3+}$ red phosphor was 70.8% and the color purity was as high as 99%. Furthermore, decay dynamics revealed that with the increase in the content of $Eu^{3+}$, the lifetimes decreased due to the increase in non-radiative transition. Importantly, the present $Na_2Gd_2B_2O_7$:0.35$Eu^{3+}$ phosphors also exhibited good thermal stability, and the emission intensity at 150 °C was about 56% of that at 30 °C. Furthermore, a warm white light-emitting diode (WLED) device was fabricated with commercial $BaMgAl_{10}O_{17}$:$Eu^{2+}$ blue phosphors, $(Ba,Sr)_2(SiO_4)$:$Eu^{2+}$ green phosphors, and the as-prepared $Na_2Gd_2B_2O_7$:0.35$Eu^{3+}$ red phosphors as well as a 395 nm LED chip. The device exhibited CIE coordinates of (0.4367, 0.3987), a high color rendering index (CRI = 92.2), a low correlated color temperature (CCT = 2960 K), and a luminous efficacy of 40.65 lm $W^{-1}$. The observed results strongly indicate that the as-prepared $Na_2Gd_2B_2O_7$:$Eu^{3+}$ phosphors may be used as the red emitting component in pc-WLEDs.

Received 6th August 2018
Accepted 9th September 2018

DOI: 10.1039/c8ra06607h

rsc.li/rsc-advances



## Introduction

The design and development of novel rare-earth doped phosphors are critical areas studied around the world for encountering the energy crisis.[1–4] Phosphor-converted white light-emitting diodes (pc-WLEDs) are a boon for solid-state lighting.[5–8] The outstanding advantages of pc-WLEDs, such as low power consumption, enhanced lifetime (>100 000 h), durability, affordability and compact design, make them promising candidates to replace traditional incandescent, fluorescent and discharge lamps.[8,9] The pc-WLED applications have experienced exponential growth in the areas of indoor and outdoor lighting.[10,11] In past decades, the pc-WLEDs have been fabricated *via* different approaches. Among these, a blue LED (InGaN) chip coated with cerium-doped yttrium aluminum garnet (YAG:$Ce^{3+}$) yellow phosphors produced white light.[12,13] However, the device exhibits a low color-rendering index (CRI) and high correlated color temperature (CCT) due to the lack of red color[14–16] To overcome these shortcomings, hybridizing tri-color phosphors was introduced to develop the pc-WLEDs.[17,18] The blended tri-color phosphors emit white light when excited by near ultraviolet (UV) photons.[19] Moreover, for indoor lighting applications, high CRI and low CCT are the two crucial factors.[20] Therefore, the development of novel high-efficiency red-emitting phosphors is important and has gained considerable attention.

Rare earth-activated red-emitting phosphors such as $Y_2O_3$:$Eu^{3+}$ and $Y_2O_3S$:$Eu^{3+}$ have been commercialized.[21] However, the unstable nature of this sulfide-based phosphor under ambient environment highly restricts the device performance during long-time operation. These problems could be addressed through the discovery of a novel red emitting phosphor which should possess high stability.[15] Moreover, the $Eu^{3+}$ ions exhibit better narrow red emissions among the discovered rare earth ions.[22–28] $Eu^{3+}$ ions show two prominent characteristic emission peaks in the orange-red and pure red regions due to the $^5D_0 \rightarrow {}^7F_1$ and $^5D_0 \rightarrow {}^7F_2$ intra-configurational transitions, respectively.[29] In addition, the phosphor emission is strongly correlated to chemical surroundings around the crystallographic site. As seen from the literature, $Eu^{3+}$ ion-activated phosphor emits two distinct colors, which are induced from magnetic–dipole transition ($^5D_0 \rightarrow {}^7F_1$) and electric–dipole transition ($^5D_0 \rightarrow {}^7F_2$).[30] If the activator prefers the inversion

*College of Physics and Optoelectronics, Taiyuan University of Technology, Taiyuan 030024, P. R. China. E-mail: huangxy04@126.com*

symmetry site, the magnetic–dipole transition ($^5D_0 \rightarrow {}^7F_1$) will dominate, resulting in orange-red emission.[31] On the contrary, when the dopant ions occupy a non-inversion symmetry site, the resulting phosphors will exhibit pure red emissions because the electric–dipole transition ($^5D_0 \rightarrow {}^7F_2$) dominates.[32] Thus, the selection of host materials is a crucial factor and decides the final emission color of the phosphor. Accordingly, different inorganic host materials such as sulfides, oxysulfides, nitrides, phosphates, silicates, borates and aluminates families have been studied for developing inorganic phosphors.[33–36] Among these, borates have attracted much interest due to their inherent physical and chemical properties, such as good thermal stability, large band-gap, ultraviolet (UV) transparency, and high luminescence efficiency.[37] $Na_2Gd_2B_2O_7$ is an important class of alkali earth borate phosphor.[38] To the best of our knowledge, the synthesis and luminescence properties of $Eu^{3+}$-doped $Na_2Gd_2B_2O_7$ phosphors have not been reported so far.

Hence, in the present study, we prepared novel $Na_2Gd_2B_2O_7$:$Eu^{3+}$ phosphors doped with different concentrations of $Eu^{3+}$ ions. The photoluminescence behaviors of the $Na_2Gd_2B_2O_7$:$Eu^{3+}$ phosphors were studied through complementary analyses such as photoluminescence excitation (PLE), photoluminescence emission (PL), color coordinates, color purity, internal quantum efficiency (IQE), luminescence lifetimes, and temperature-dependent emission spectra. Moreover, a warm WLED device was fabricated and the device performance was studied under the excitation of near-UV light. The acquired aforementioned results for the $Na_2Gd_2B_2O_7$:$Eu^{3+}$ phosphors are discussed and compared with earlier published reports.

## Experimental

Powder samples of pristine $Na_2Gd_2B_2O_7$ and $Na_2(Gd_{1-x}Eu_x)_2B_2O_7$ (abbreviated as: $Na_2Gd_2B_2O_7$:$xEu^{3+}$; $x = 0$, 0.05, 0.15, 0.35, 0.45, and 0.50) phosphors were synthesized by a solid-state reaction method. The raw materials were $Na_2CO_3$ (analytical reagent, AR), $H_3BO_3$ (AR), $Eu_2O_3$ (99.99%), and $Gd_2O_3$ (99.99%). These raw materials were stoichiometrically weighed and homogeneously mixed for 15 min using an agate mortar. The homogeneous mixture powder was placed in a covered alumina crucible and kept in the muffle furnace. The muffle furnace was operated at 980 °C for 6 h at ambient atmosphere. Subsequently, the sintered samples were cooled to room temperature and again ground for 15 min to acquire fine particles. The obtained phosphors were further used for characterizations.

The phase and structural information of the as-prepared $Na_2Gd_2B_2O_7$ and $Na_2Gd_2B_2O_7$:0.35$Eu^{3+}$ phosphors were obtained *via* powder X-ray diffraction (XRD) using a Bruker D8 Advance diffractometer with Cu-K$\alpha$ radiation source. The morphology and elemental distribution of the $Na_2Gd_2B_2O_7$:0.35$Eu^{3+}$ phosphors were analyzed using field emission scanning electron microscopy (FE-SEM, MAIA3 TESCA). Room temperature PLE and PL spectra were analyzed using an Edinburgh FS5 fluorescence spectrophotometer equipped with a 150 W Xenon lamp as the excitation source. Color coordinates of the phosphors were examined with the Commission International de I'Eclairage (CIE 1931) color chromaticity system. Furthermore, the IQE was analyzed in integrating sphere mode using commercial $BaSO_4$ as reference. The decay lifetimes of the $Na_2Gd_2B_2O_7$:$Eu^{3+}$ phosphors were measured by recording decay profiles using the same spectrophotometer and pulse Xenon lamp as an excitation source. Temperature-dependent PL measurements were performed from room temperature to 480 K with 20 K intervals. The temperature was precisely controlled by a digital temperature controller.

The prototype warm WLED device was assembled by blending commercial $BaMgAl_{10}O_{17}$:$Eu^{2+}$ (BAM:$Eu^{2+}$) blue phosphors, commercial $(Ba,Sr)_2(SiO_4)$:$Eu^{2+}$ green phosphors, the as-synthesized $Na_2Gd_2B_2O_7$:0.35$Eu^{3+}$ red phosphors and a 365 nm near-UV LED chip. The three phosphors were mixed homogenously with epoxy resin and the mixture was coated on the LED chip surface. Subsequently, the device performance was examined with different forward basis currents: 20, 40, 60, 80, 100 and 120 mA.

## Results and discussion

In order to analyze the phase purity and structure of the phosphor, XRD measurements were performed for the pure $Na_2Gd_2B_2O_7$ and $Na_2Gd_2B_2O_7$:0.35$Eu^{3+}$ phosphors (Fig. 1). The diffraction peaks of the as-synthesized pure $Na_2Gd_2B_2O_7$ were well matched with those in the JCPDS file No 89-4442.[38] The crystal structure of the $Na_2Gd_2B_2O_7$ compound was found to possess a monoclinic phase with space group $P2_1/c$.[39] Furthermore, on addition of $Eu^{3+}$ ions into $Na_2Gd_2B_2O_7$ host material, the observed diffraction peaks were identical to those of pure $Na_2Gd_2B_2O_7$. This result indicated that $Eu^{3+}$ doping does not impact the phosphor structure since no impurity peak was observed.

Moreover, in order to better understand the crystal structure of the $Na_2Gd_2B_2O_7$:0.35$Eu^{3+}$ phosphor, refinement analysis was performed using Fullprof program. Fig. 2(a) illustrates the structure refinement of $Na_2Gd_2B_2O_7$:0.35$Eu^{3+}$ phosphors and their crystallographic parameters are shown in Table 1. There is a good agreement between the observed and calculated XRD patterns. The crystal structure of the $Na_2Gd_2B_2O_7$:0.35$Eu^{3+}$

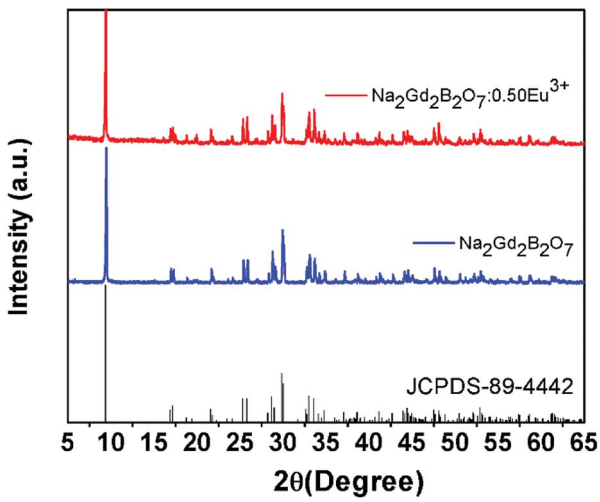


Fig. 1 X-ray diffraction patterns of the $Na_2Gd_2B_2O_7$ and $Na_2Gd_2B_2O_7$:0.35$Eu^{3+}$ phosphors.

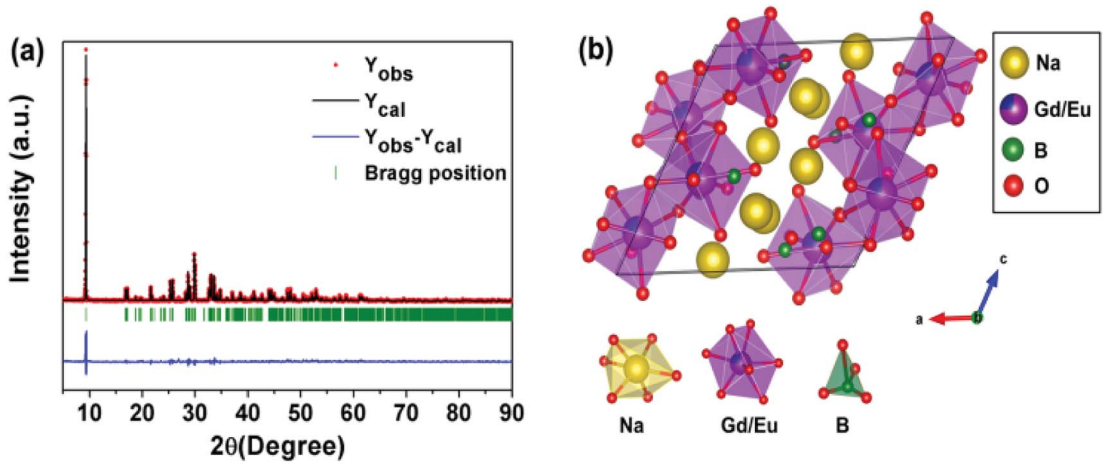


Fig. 2 (a) Rietveld refinement of XRD data of $Na_2Gd_2B_2O_7$:0.35$Eu^{3+}$ and (b) crystal structure of the $Na_2Gd_2B_2O_7$:$Eu^{3+}$ phosphor.

Table 1 Refined crystallographic parameters of $Na_2Gd_2B_2O_7$:0.35$Eu^{3+}$

| Formula | $Na_2Gd_2B_2O_7$:0.35$Eu^{3+}$ |
|---|---|
| Crystal system | Monoclinic |
| Space group | $P121/c1$ |
| $a$ | 10.6902(3) Å |
| $b$ | 6.31743(19) Å |
| $c$ | 10.3205(3) Å |
| $\alpha$ | 90° |
| $\gamma$ | 90° |
| $\beta$ | 117.806(2) |
| $V$ | 616.51(3) Å$^3$ |
| $R_{p\%}$ | 12.64 |
| $R_{wp\%}$ | 17.66 |

phosphor is shown in Fig. 2(b). In this compound, the sodium atoms have six-fold Na(1) coordination, while the boron atom has triangular coordination. The lanthanide ions may settle in the center of the distorted $LnO_8$ triangulated dodecahedra.

The FE-SEM micrograph images of the $Na_2Gd_2B_2O_7$:0.35$Eu^{3+}$ phosphors are shown in Fig. 3(a). The morphology of the phosphor was irregular and agglomerated with particle size of few micrometers. The histogram of the particle size distribution was calculated and shown in Fig. 3(b). The calculated average particle size was 1.6 μm. Elemental mapping results are presented in Fig. 3(c–h). Clearly, elements Na, Gd, B, O and Eu are observed. Furthermore, these elements are homogeneously distributed in the particles of the $Na_2Gd_2B_2O_7$:0.35$Eu^{3+}$ phosphors.

Fig. 4(a) shows the PLE and PL spectra of the $Na_2Gd_2B_2O_7$:0.35 $Eu^{3+}$ phosphors. The PLE spectrum of the $Na_2Gd_2B_2O_7$:0.35$Eu^{3+}$ phosphor was monitored at 621 nm. The PLE spectrum of the $Na_2Gd_2B_2O_7$:0.35$Eu^{3+}$ phosphor was composed of a single broad band and several distinct sharp lines. This broad excitation band located within the region of 240–310 nm was ascribed to the $O^{2-} \rightarrow Eu^{3+}$ charge transfer band.[40] The sharp distinct PLE peaks at 321, 363, 382, 395, 417 and 466 nm were due to the 4f–4f forbidden transitions of $Eu^{3+}$ ions, corresponding to the transitions of $^7F_0 \rightarrow {}^5H_6$, $^7F_0 \rightarrow {}^5D_4$, $^7F_0 \rightarrow {}^5L_7$, $^7F_0 \rightarrow {}^5L_6$, $^7F_0 \rightarrow {}^5D_3$, and $^7F_0 \rightarrow {}^5D_2$. The $^7F_0 \rightarrow {}^5L_6$ transition at 395 nm had the highest intensity. These PLE results depicted that the as-prepared $Na_2Gd_2B_2O_7$:$Eu^{3+}$ phosphors would be appropriate candidates for pc-WLEDs device

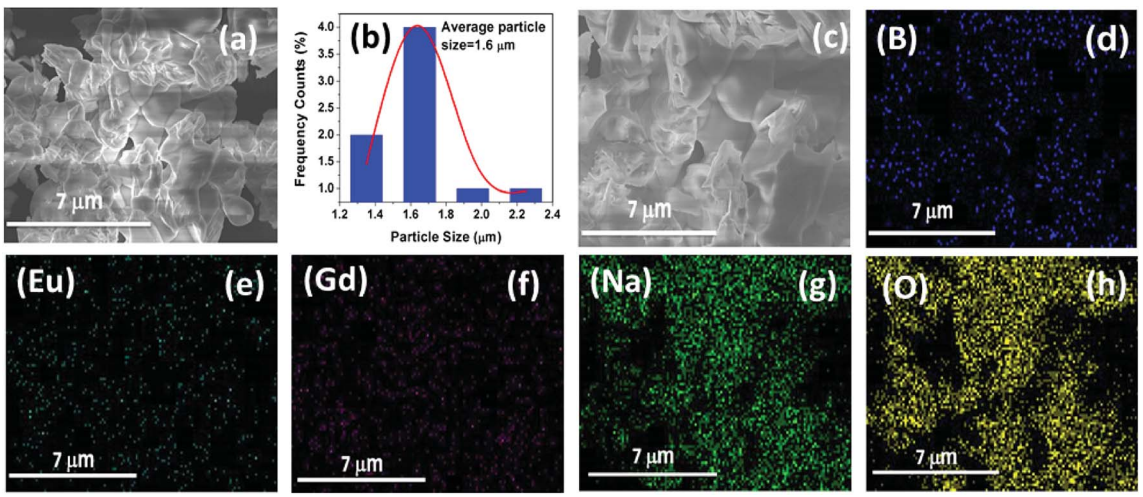


Fig. 3 (a) SEM image, (b) histogram of the particle size distribution, and (c–h) elemental mapping of $Na_2Gd_2B_2O_7$:0.35$Eu^{3+}$ phosphors.

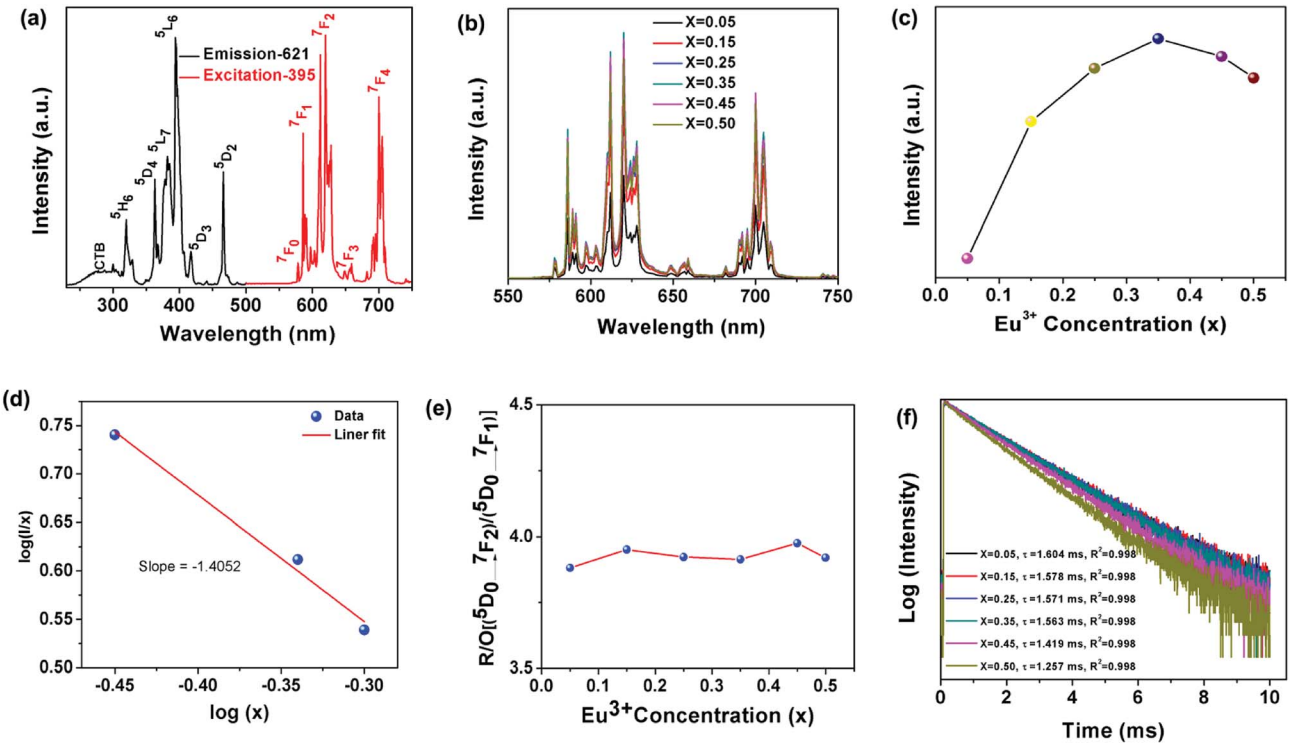


Fig. 4 (a) PLE spectrum and PL spectra of $Na_2Gd_2B_2O_7$:0.35$Eu^{3+}$ phosphors. (b) PL spectra of $Na_2Gd_2B_2O_7$:x$Eu^{3+}$ phosphors with different $Eu^{3+}$ concentrations ($x = 0.05$, 0.15, 0.25, 0.35, 0.45, and 0.50). (c) Influence of the $Eu^{3+}$ concentration on the emission intensity. (d) Plot of log($I/x$) *vs.* log($x$) for the $Eu^{3+}$ 621 nm emission in $Na_2Gd_2B_2O_7$:x$Eu^{3+}$ phosphors. (e) The integrated intensity ratio (R/O) of [($^5D_0 \rightarrow {}^7F_2$)/($^5D_0 \rightarrow {}^7F_1$)] as a function of $Eu^{3+}$ concentrations in $Na_2Gd_2B_2O_7$:x$Eu^{3+}$ phosphors. (f) Decay curves of $Na_2Gd_2B_2O_7$:$Eu^{3+}$ phosphors monitored at 621 nm with an excitation wavelength of 395 nm.

pumped by near-UV light.[41] As shown in Fig. 4(a), upon excitation at 395 nm, the obtained PL spectrum displays a group of narrow emissions centered at 577, 585, 621, 659, and 700 nm due to the transitions of $^5D_0 \rightarrow {}^7F_0$, $^5D_0 \rightarrow {}^7F_1$, $^5D_0 \rightarrow {}^7F_2$, $^5D_0 \rightarrow {}^7F_3$, and $^5D_0 \rightarrow {}^7F_4$, respectively.[42] The primary $^5D_0 \rightarrow {}^7F_2$ transition is known as the magnetic dipole (MD) transition, while the $^5D_0 \rightarrow {}^7F_1$ transition belongs to the electric dipole (ED) transition. The MD transition is strongly influenced by the surrounding chemical environment. In sharp contrast, the ED transition is independent of the coordination surroundings around the crystallographic site.[43] However, the dopant ($Eu^{3+}$) ions can occupy either an inversion symmetry site or a site without inversion symmetry in the host lattice. When the $Eu^{3+}$ ions occupy an inversion symmetry site in a coordination surrounding, the $^5D_0 \rightarrow {}^7F_1$ transition has higher intensity than the $^5D_0 \rightarrow {}^7F_2$ transition, and the $Eu^{3+}$ ions exhibit orange-red emission.[44] Similarly, when $Eu^{3+}$ ions occupy a crystallographic site without inversion symmetry, the red emission due to $^5D_0 \rightarrow {}^7F_2$ transition will be dominant and thus, the $Eu^{3+}$ ions will produce pure red emissions.[45] In $Na_2Gd_2B_2O_7$:0.35$Eu^{3+}$ phosphors, the red emission at 621 nm, owing to the $^5D_0 \rightarrow {}^7F_2$ transition, exhibited the highest emission intensity; therefore, the $Eu^{3+}$ ions occupied sites without inversion symmetry in the $Na_2Gd_2B_2O_7$ host lattice.

In order to obtain the relationship between PL intensity and $Eu^{3+}$ concentration, PL spectra of the $Na_2Gd_2B_2O_7$:x$Eu^{3+}$ phosphors with various concentrations of $Eu^{3+}$ ions were measured and shown in Fig. 4(b). The profiles of the obtained PL spectra were almost identical and no peak shift was observed. Moreover, with an increase in the $Eu^{3+}$ concentration, the PL intensity increased accordingly until $x = 0.35$, as shown in Fig. 4(c). Furthermore, when the $Eu^{3+}$ concentration was above $x = 0.35$, the PL intensity decreased due to concentration quenching.[46]

Concentration quenching was observed owing to the non-radiative energy transfer to the neighbouring $Eu^{3+}$ ions. The concentration quenching mechanism is highly influenced by the critical distance ($R_c$) between neighbouring $Eu^{3+}$ ions. Based on $R_c$ values, the energy transfer for concentration quenching can be involved in different mechanisms. When $R_c$ is less than 5 Å, the mechanism for concentration quenching can be attributed to an exchange interaction. When $R_c$ exceeded 5 Å, electric multipolar interaction would be the mechanism for concentration quenching. To calculate the $R_c$ values of the $Na_2Gd_2B_2O_7$:$Eu^{3+}$ phosphors, the following expression was used:[47]

$$R_c = 2\left[\frac{3V}{4\pi X_C Z}\right]^{\frac{1}{3}} \text{Å} \quad (1)$$

where $V$ is the volume of the unit cell, $X_C$ refers the activator critical doping concentration and $Z$ represents the number of formula units per unit cell. For $Na_2Gd_2B_2O_7$:$Eu^{3+}$ phosphors, $V = 617.5$ Å, $X_C = 0.35$ and $Z = 4$. The obtained $R_c$ was 9.4 Å, which was higher than 5 Å. Thus, the concentration quenching mechanism should be the electric multipolar interaction in $Na_2Gd_2B_2O_7$:$Eu^{3+}$ phosphors. Moreover, the detailed energy

transfer mechanism for concentration quenching can be examined using the following expression:[15]

$$\frac{I}{X} = K\left[1 + \beta(x)^{\frac{\theta}{3}}\right]^{-1} \quad (2)$$

where $I$ is the emission intensity, $X$ denotes the dopant concentration, $K$ and $\beta$ are constants for the given host at the same excitation, $\theta$ is a constant for multipolar interaction, which varies between 6, 8 and 10, corresponding to the electric dipole–dipole, dipole–quadrupole, and quadrupole–quadrupole interactions, respectively.[48,49] $\theta$ can be estimated from the plot of $\log(I/x)$ *vs.* $\log(x)$. Fig. 4(d) represents the plot of $\log(I/x)$ *vs.* $\log(x)$, and the experimental data were effectively linearly fitted. The slope of the line was found to be −1.3 and the calculated $\theta$ was 4.2. The determined $\theta$ is close to 3 and hence, luminescence quenching mechanism could be attributed to the nonradiative energy transfer among the nearest neighbors.[15,22,50–52]

In addition, the integrated red/orange (R/O) emission intensity ratio of the ($^5D_0 \rightarrow {}^7F_2$) and ($^5D_0 \rightarrow {}^7F_1$) transitions was calculated to understand the site symmetry of the $Na_2Gd_2B_2O_7$:$Eu^{3+}$ phosphors. Fig. 4(e) illustrates the R/O intensity ratio of [($^5D_0 \rightarrow {}^7F_2$)/($^5D_0 \rightarrow {}^7F_1$)] as a function of $Eu^{3+}$ concentration in the $Na_2Gd_2B_2O_7$:$xEu^{3+}$ phosphors. The calculated intensity ratio was 3.8, 3.9, 3.9, 3.9, 3.9 and 3.9 for $x = 0.05$, 0.15, 0.25, 0.35, 0.45 and 0.50, respectively. The calculated R/O was higher than unity for all the samples. This result further proves that the $Eu^{3+}$ ion occupies non-centrosymmetric sites in the $Na_2Gd_2B_2O_7$:$Eu^{3+}$ phosphors.

The decay curves of $Na_2Gd_2B_2O_7$:$xEu^{3+}$ phosphors with different $Eu^{3+}$ concentrations were measured upon excitation at 395 nm and by monitoring the emission at 621 nm, as presented in Fig. 4(f). The measured decay curves were well fitted with the first-order exponential equation, and the lifetimes of 621 nm emission were determined by the following expression:[53]

$$I_t = I_0 + A\exp\left(\frac{-t}{\tau}\right) \quad (3)$$

where $I_0$ denotes emission intensity at $t = 0$, $I_t$ refers the emission intensity at time $t$, $A$ is the decay constant, and $\tau$ is the average lifetime. From the decay curves, the average lifetimes were calculated as 1.604, 1.578, 1.571, 1.563, 1.419 and 1.257 ms for the samples with $Eu^{3+}$ concentrations of $x = 0.05$, 0.15, 0.25, 0.35, 0.45 and 0.50, respectively. The calculated lifetimes of the $Na_2Gd_2B_2O_7$:$xEu^{3+}$ phosphors were found to be in the millisecond range and the single exponential fitting revealed that the $Eu^{3+}$ ions may be occupied in mono sites.[54] The obtained fluorescence lifetime was decreased with the increase in the concentration of $Eu^{3+}$ ions. By increasing the concentration of $Eu^{3+}$ ions, the distance between the neighbouring $Eu^{3+}$ ions will be reduced and the energy will be transferred through a non-radiative pathway.

Color coordinates of the $Na_2Gd_2B_2O_7$:$xEu^{3+}$ phosphors were analyzed using computer imaging software given in CIE 1931 (Commission Internationale de l'Eclairage) color chromaticity diagram. The calculated CIE coordinates were shown to be (0.650, 0.349), (0.652, 0.347), (0.652, 0.347), (0.652, 0.347), (0.653, 0.346) and (0.652, 0.346) for $x = 0.05$, 0.15, 0.25, 0.35, 0.45 and 0.50, respectively. Fig. 5 denotes the CIE coordinates of the $Na_2Gd_2B_2O_7$:$0.35Eu^{3+}$ phosphors, commercial $Y_2O_3$:$Eu^{3+}$ phosphors and National Television Standard Committee (NTSC) for red phosphors. Clearly, the CIE coordinates of the $Na_2Gd_2B_2O_7$:$0.35Eu^{3+}$ phosphor [CIE: (0.652, 0.347)] were close to that of NTSC red phosphors [CIE: (0.67, 0.33)], and was better than that of the commercial $Y_2O_2S$:$Eu^{3+}$ phosphor [CIE: (0.63, 0.35)].[55] Furthermore, the inset in Fig. 5 shows the digital images of the as-prepared $Na_2Gd_2B_2O_7$:$0.35Eu^{3+}$ phosphors' illumination under natural sunlight and a 365 nm UV lamp. Upon UV light exposure, the phosphors emitted pure red color.

Furthermore, to better understand the phosphor emission, the color purity of the $Na_2Gd_2B_2O_7$:$0.35Eu^{3+}$ phosphor was calculated using the given equation:[56]

$$\text{Color purity} = \frac{\sqrt{(x - x_{ee})^2 + (y - y_{ee})^2}}{\sqrt{(x_d - x_{ee})^2 + (y_d - y_{ee})^2}} \times 100\% \quad (4)$$

where $(x, y)$ refers to the CIE coordinates of the $Na_2Gd_2B_2O_7$:$0.35Eu^{3+}$ phosphor, $(x_d, y_d)$ expresses the CIE coordinates of the dominant wavelength points and $(x_{ee}, y_{ee})$ refers to the CIE coordinates of white illumination. The obtained values of ($x = 0.652$, $y = 0.347$), ($x_d = 0.655$, $y_d = 0.347$) and ($x_{ee} = 0.310$, $y_{ee} = 0.316$) were substituted in the above expression. The calculated color purity of the $Na_2Gd_2B_2O_7$:$0.35Eu^{3+}$ phosphor was about 99%. These results indicated that $Na_2Gd_2B_2O_7$:$0.35Eu^{3+}$ phosphors had high color purity and admirable CIE coordinates.

In addition, the IQE of $Na_2Gd_2B_2O_7$:$0.35Eu^{3+}$ phosphor was determined. Fig. 6(a) represents the excitation line and the emission spectrum of $BaSO_4$ and $Na_2Gd_2B_2O_7$:$0.35Eu^{3+}$ phosphors. The IQE was determined using the following expression:[57]

$$\eta_{QE} = \frac{\int L_S}{\int E_R - \int E_S}\% \quad (5)$$

where $L_S$ denotes the emission spectrum of the sample, $E_R$ refers the excitation light spectrum without sample, and $E_S$ indicates the

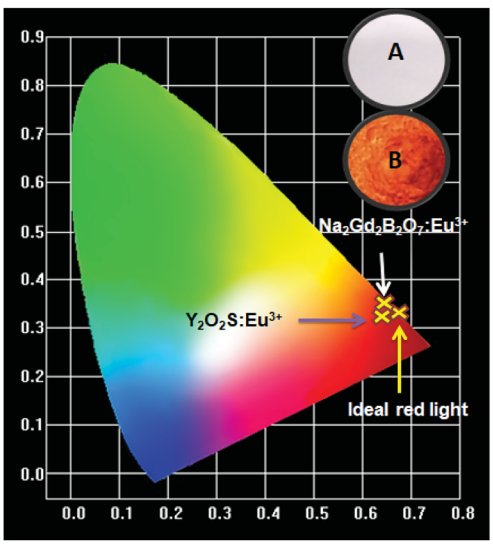


Fig. 5 CIE chromaticity diagram of $Na_2Gd_2B_2O_7$:$0.35Eu^{3+}$ and $Y_2O_2S$:$Eu^{3+}$ phosphors. Inset: photographs of $Na_2Gd_2B_2O_7$:$0.35Eu^{3+}$ under daylight (A) and 365 nm UV lamp (B).

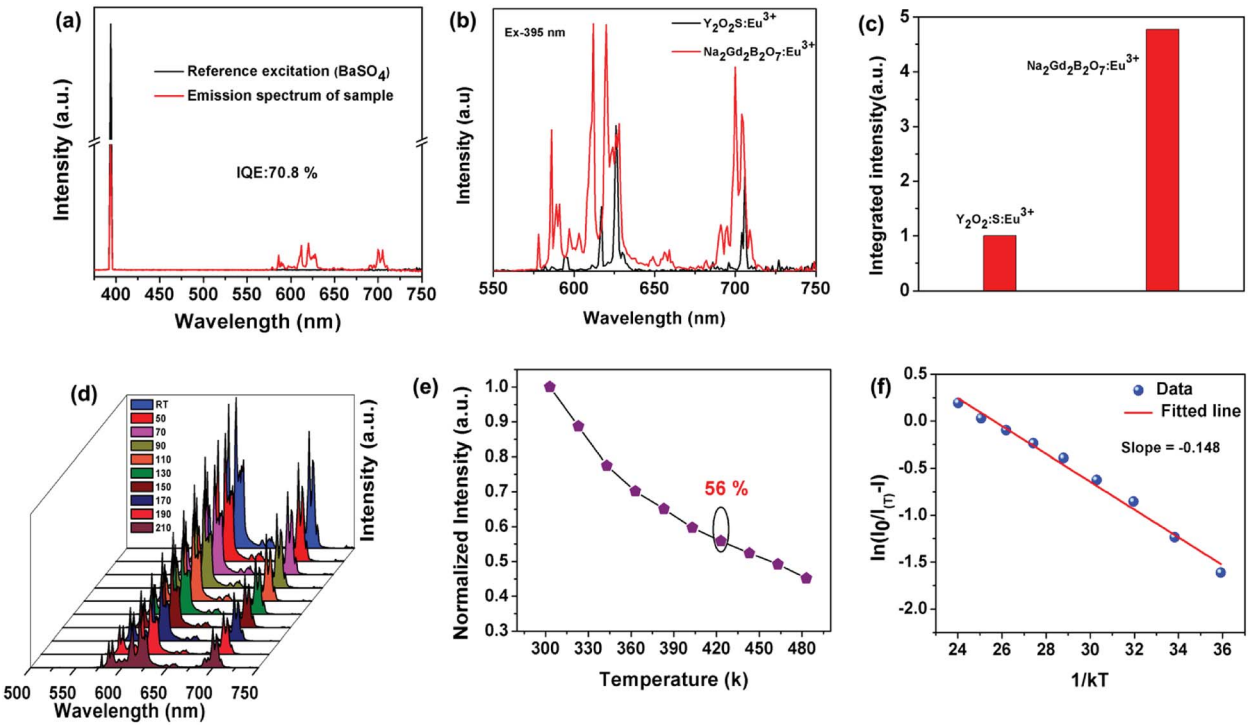


Fig. 6 (a) Excitation line of $BaSO_4$ and the emission spectrum of $Na_2Gd_2B_2O_7$:0.35$Eu^{3+}$ phosphors collected using an integrating sphere. (b) The PL spectra of the as-prepared $Na_2Gd_2B_2O_7$:0.35$Eu^{3+}$ and commercial $Y_2O_2S:Eu^{3+}$ phosphors under 395 nm excitation. (c) Comparison of the integrated PL intensity of the as-prepared $Na_2Gd_2B_2O_7$:0.35$Eu^{3+}$ and commercial $Y_2O_2S:Eu^{3+}$ phosphors excited at 395 nm. (d) Temperature-dependent PL spectra of $Na_2Gd_2B_2O_7:Eu^{3+}$ phosphors excited at 395 nm. (e) Normalized PL emission intensity at different temperatures. (f) The linear fitting curve of $\ln(I_0/I-1)$ *versus* $1/kT$ for the $Na_2Gd_2B_2O_7:Eu^{3+}$ phosphors.

spectrum of the light used to excite the sample. Accordingly, the calculated IQE of the $Na_2Gd_2B_2O_7$:0.35$Eu^{3+}$ phosphor was 70.8%. The obtained IQE was greater than some previously reported $Eu^{3+}$-activated red phosphors, such as $Ba_2SiO_4$ (IQE: 55%), and $LiGdF_4$:Eu (IQE: 32%).[58,59] Moreover, the PL spectrum of the $Na_2Gd_2B_2O_7$:0.35$Eu^{3+}$ phosphor was compared with that of the commercial $Y_2O_2S:Eu^{3+}$ phosphor under excitation of 395 nm, as shown in Fig. 6(b). It can be seen from Fig. 6(c) that the integrated PL intensity of the $Na_2Gd_2B_2O_7$:0.35$Eu^{3+}$ phosphor was about 4.7-fold higher than that of commercial $Y_2O_2S:Eu^{3+}$ red phosphor.[60,61] Thermal stability of the $Na_2Gd_2B_2O_7$:0.35$Eu^{3+}$ sample was examined from room temperature to 210 °C upon excitation of 395 nm. The temperature-dependent PL spectra are illustrated in Fig. 6(d). Clearly, no apparent shift was observed in the peaks in the PL spectra with the increase in the temperature. On the contrary, the emission intensity declines with the increase in the temperature owing to thermal quenching caused by non-radiative transitions.

As seen in Fig. 6(e), the emission intensity at 150 °C (423 K) is approximately 56% of that at room temperature. This value is higher than that obtained for some previously reported $Eu^{3+}$ ion-activated red phosphors, such as $LaSiO_2N:Eu^{3+}$ (42.3%) and $Gd_2ZnTiO_6:Eu^{3+}$ (51%).[62,63]

Furthermore, the activation energy of the $Na_2Gd_2B_2O_7$:0.35-$Eu^{3+}$ phosphors was determined using the following expression:[47]

$$I = I_0[1 + c\ \exp(-E_a/kT)]^{-1}\ \text{eV}^{-1} \quad (6)$$

where $I_0$ is referred to as room temperature PL intensity, $c$ is a constant for any given host, $k$ refers the Boltzmann constant ($8.62 \times 10^{-5}$ eV), and $I$ is the PL intensity at a periodic temperature interval. The plot between $\ln(I_0/I-1)$ *vs.* $1/kT$ is shown in Fig. 6(f) and the data is effectively linearly fitted with a slope of −0.148. Then, the activation energy of thermal quenching for the $Na_2Gd_2B_2O_7$:0.35$Eu^{3+}$ phosphor was calculated to be 0.148 eV.[64,65] Thus, the temperature-dependent PL

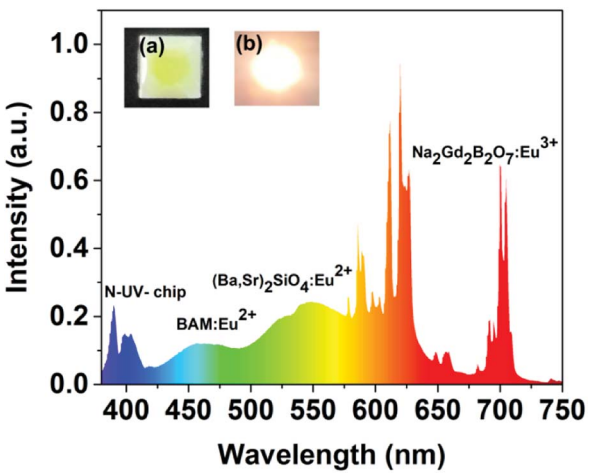


Fig. 7 Electroluminescence spectrum of the as-fabricated WLED lamp with 395 nm near-UV chip and BAM:$Eu^{2+}$, $(Ba_2Sr)_2SiO_4:Eu^{2+}$ and $Na_2Gd_2B_2O_7:Eu^{3+}$ phosphors driven by 20 mA.

studies strongly emphasized that the $Na_2Gd_2B_2O_7$:0.35$Eu^{3+}$ phosphors have outstanding thermal properties.

In order to realize practical applications, a WLED device was fabricated using a 395 nm UV LED chip and phosphor blends of commercial BAM:$Eu^{2+}$ blue phosphors, commercial $(Ba,Sr)_2(SiO_4)$:$Eu^{2+}$ green phosphors and the as-synthesized $Na_2Gd_2B_2O_7$:0.35$Eu^{3+}$ red phosphors. Fig. 7 shows the electroluminescence (EL) spectrum of the fabricated WLED device under an operating current of 20 mA. Digital photographs of WLED with and without driving current are shown in the inset of Fig. 7. The obtained CIE coordinates, CCT, CRI, and luminous efficacy were found to be (0.4367, 0.3987), 2960 K, 92.2, and 40.65 lm $W^{-1}$, respectively. These results suggest that the $Na_2Gd_2B_2O_7$:0.35$Eu^{3+}$ red emitting phosphor may be applied in warm LEDs for indoor lighting.

## Conclusions

In conclusion, we successfully prepared a series of novel red emitting $Na_2Gd_2B_2O_7$:$x$$Eu^{3+}$ phosphors through solid state reactions. The excitation spectra evidenced that the phosphor could be efficiently excited by near-UV light. The $Eu^{3+}$ ions occupied the non-centrosymmetric lattice site since the phosphor showed pure red emission at around 621 nm. The optimal dopant concentration of $Eu^{3+}$ ions in $Na_2Gd_2B_2O_7$:$x$$Eu^{3+}$ phosphors was $x = 0.35$ and the corresponding critical distance ($R_c$) was found to be 9.4 Å. The color coordinates and color purity of the $Na_2Gd_2B_2O_7$:0.35$Eu^{3+}$ phosphors were found to be (0.652, 0.347) and 99%, respectively. The measured IQE was 70.8% for the $Na_2Gd_2B_2O_7$:0.35$Eu^{3+}$ phosphor and its integrated PL intensity was 4.7-fold higher than that of the commercial $Y_2O_2S$:$Eu^{3+}$ red phosphor. At 150 °C, the emission intensity remained at approximately 56% of that at room temperature. Finally, a warm WLED device was fabricated with commercial $BaMgAl_{10}O_{17}$:$Eu^{2+}$ blue phosphors, $(Ba,Sr)_2(SiO_4)$:$Eu^{2+}$ green phosphors, and the as-prepared $Na_2Gd_2B_2O_7$:0.35$Eu^{3+}$ red phosphors as well as a 395 nm LED chip. The device showed CIE coordinates of (0.4367, 0.3987), high CRI (92.2), low CCT (2960 K), and luminous efficacy of 40.65 lm $W^{-1}$. The overall results indicated that the $Na_2Gd_2B_2O_7$:$Eu^{3+}$ phosphors could be favorable red phosphor candidates for the application in pc-WLEDs under near-UV excitation.

## Conflicts of interest

There are no conflicts to declare.

## Acknowledgements

This study was supported by the National Natural Science Foundation of China (No. 51502190), the Program for the Outstanding Innovative Teams of Higher Learning Institutions of Shanxi, and the Open Fund of the State Key Laboratory of Luminescent Materials and Devices (South China University of Technology, No. 2017-skllmd-01).

## Notes and references

1 X. Huang, *Nat. Photonics*, 2014, **8**, 748–749.
2 X. Huang, *J. Alloys Compd.*, 2017, **690**, 356–359.
3 P. Du, L. Luo, X. Huang and J. S. Yu, *J. Colloid Interface Sci.*, 2018, **514**, 172–181.
4 P. Du, X. Huang and J. S. Yu, *Inorg. Chem. Front.*, 2017, **4**, 1987–1995.
5 Z.-w. Zhang, L.-j. Wang, S.-s. Yang, W.-g. Chen and X.-j. Chu, *Dyes Pigm.*, 2017, **142**, 272–276.
6 X. Huang, B. Li, H. Guo and D. Chen, *Dyes Pigm.*, 2017, **143**, 86–94.
7 X. Huang and H. Guo, *Dyes Pigm.*, 2018, **152**, 36–42.
8 X. Huang, J. Liang, B. Li, L. Sun and J. Lin, *Opt. Lett.*, 2018, **43**, 3305–3308.
9 L. Sun, H. Guo, J. Liang, B. Li and X. Huang, *J. Lumin.*, 2018, **202**, 403–408.
10 K. Park, H. Kim and D. Hakeem, *Dyes Pigm.*, 2017, **136**, 70–77.
11 X. Huang, B. Li and H. Guo, *J. Alloys Compd.*, 2017, **695**, 2773–2780.
12 Y. Chu, Q. Zhang, Y. Li, Z. Liu, J. Xu, H. Zeng and H. Wang, *J. Alloys Compd.*, 2017, **693**, 308–314.
13 X. Huang, H. Guo and B. Li, *J. Alloys Compd.*, 2017, **720**, 29–38.
14 T. Sreena, P. P. Rao, A. K. Raj and T. A. Thara, *J. Alloys Compd.*, 2018, **751**, 148–158.
15 X. Huang and H. Guo, *RSC Adv.*, 2018, **8**, 17132–17138.
16 Y. Wang, J. Ding, Y. Li, L. Yang, X. Ding and Y. Wang, *RSC Adv.*, 2016, **6**, 42618–42626.
17 H. Guo, X. Huang and Y. Zeng, *J. Alloys Compd.*, 2018, **741**, 300–306.
18 P. Du, Y. Hua and J. S. Yu, *RSC Adv.*, 2018, **8**, 26676–26681.
19 S. Zhang, H. Luo, Z. Mu, J. Li, S. Guo, Z. Li, Q. Wang and F. Wu, *J. Alloys Compd.*, 2018, **757**, 423–433.
20 X. Huang and H. Guo, *Dyes Pigm.*, 2018, **154**, 82–86.
21 M. Xie, Y. Li and R. Li, *J. Lumin.*, 2013, **136**, 303–306.
22 H. Deng, Z. Gao, N. Xue, J. H. Jeong and R. Yu, *J. Lumin.*, 2017, **192**, 684–689.
23 B. Li, X. Huang, H. Guo and Y. Zeng, *Dyes Pigm.*, 2018, **150**, 67–72.
24 X. Li, D. Xu, X. Liu and H. Guo, *RSC Adv.*, 2017, **7**, 53839–53845.
25 P. Du, Y. Guo, S. H. Lee and J. S. Yu, *RSC Adv.*, 2017, **7**, 3170–3178.
26 J. Zhong, W. Zhao, L. Yang, P. Shi, Z. Liao, M. Xia, W. Pu, W. Xiao and L. Wang, *RSC Adv.*, 2018, **8**, 13054–13060.
27 L. Li, W. Chang, W. Chen, Z. Feng, C. Zhao, P. Jiang, Y. Wang, X. Zhou and A. Suchocki, *Ceram. Int.*, 2017, **43**, 2720–2729.
28 L. Li, Y. Pan, X. Zhou, C. Zhao, Y. Wang, S. Jiang, A. Suchocki and M. Brik, *J. Alloys Compd.*, 2016, **685**, 917–926.
29 Z. Zhang, D. Ma, Y. Yue, M. Ma and R. Liu, *J. Alloys Compd.*, 2015, **636**, 113–116.
30 L. Li, Y. Pan, W. Wang, Y. Zhu, W. Zhang, H. Xu, L. Zhou and X. Liu, *J. Alloys Compd.*, 2018, **731**, 496–503.

 

31 Y. Onishi, T. Nakamura, H. Sone and S. Adachi, *J. Lumin.*, 2018, **197**, 242–247.
32 K. Szczodrowski, J. Barzowska, N. Górecka and M. Grinberg, *J. Alloys Compd.*, 2018, **748**, 44–50.
33 Y. Kang, B. Thuy, Y. Shimokawa, T. Hayakawa, S. Sakaida, L. Miao, S. Tanemura, S. Honda and Y. Iwamoto, *J. Lumin.*, 2016, **169**, 78–85.
34 K. Uheda, H. Takizawa, T. Endo, H. Yamane, M. Shimada, C.-M. Wang and M. Mitomo, *J. Lumin.*, 2000, **87**, 967–969.
35 H. Yang, L. Yu, L. Shen and L. Wang, *Mater. Lett.*, 2004, **58**, 1172–1175.
36 Y. Naik, M. Mohapatra, N. Dahale, T. Seshagiri, V. Natarajan and S. Godbole, *J. Lumin.*, 2009, **129**, 1225–1229.
37 F. Xiong, J. Luo, H. Lin, X. Meng, Y. Wang, H. Shen and W. Zhu, *Optik*, 2018, **156**, 31–38.
38 C. Guo, H. Jing and T. Li, *RSC Adv.*, 2012, **2**, 2119–2122.
39 G. Corbel, M. Leblanc, E. Antic-Fidancev and M. Lemaıtre-Blaise, *J. Solid State Chem.*, 1999, **144**, 35–44.
40 Z.-w. Zhang, L.-j. Wang, X.-j. Chu, P. Zhang, Y.-j. Cao, Y.-r. Xi, W.-g. Chen and D.-j. Wang, *J. Alloys Compd.*, 2017, **695**, 3220–3224.
41 I. P. Sahu, D. Bisen, N. Brahme and R. K. Tamrakar, *J. Mater. Sci.: Mater. Electron.*, 2015, **26**, 10075–10086.
42 P. Du, X. Huang and J. S. Yu, *Chem. Eng. J.*, 2018, **337**, 91–100.
43 B. Wang, Q. Ren, O. Hai and X. Wu, *RSC Adv.*, 2017, **7**, 15222–15227.
44 X. Huang, B. Li and H. Guo, *Ceram. Int.*, 2017, **43**, 10566–10571.
45 D. Singh, S. Sheoran, V. Tanwar and S. Bhagwan, *J. Mater. Sci.: Mater. Electron.*, 2017, **28**, 3243–3253.
46 Y. Meng, W. Zhao, L. Wang, Y. Zhou, M. He and Y. Zhu, *J. Mater. Sci.: Mater. Electron.*, 2017, **28**, 4984–4989.
47 W. Ran, H. M. Noh, B. K. Moon, S. H. Park, J. H. Jeong, J. H. Kim, G. Liu and J. Shi, *J. Lumin.*, 2018, **197**, 270–276.
48 Q. Shao, H. Ding, L. Yao, J. Xu, C. Liang and J. Jiang, *RSC Adv.*, 2018, **8**, 12035–12042.
49 X. Zhang, J. Zhang and M. Gong, *Opt. Mater.*, 2014, **36**, 850–853.
50 Q. Zhang, X. Wang, X. Ding and Y. Wang, *Inorg. Chem.*, 2017, **56**, 6990–6998.
51 R. Yu, H. M. Noh, B. K. Moon, B. C. Choi, J. H. Jeong, K. Jang, S. S. Yi and J. K. Jang, *J. Alloys Compd.*, 2013, **576**, 236–241.
52 H. Li, R. Zhao, Y. Jia, W. Sun, J. Fu, L. Jiang, S. Zhang, R. Pang and C. Li, *ACS Appl. Mater. Interfaces*, 2014, **6**, 3163–3169.
53 M. Janulevicius, P. Marmokas, M. Misevicius, J. Grigorjevaite, L. Mikoliunaite, S. Sakirzanovas and A. Katelnikovas, *Sci. Rep.*, 2016, **6**, 26098.
54 L.-L. Wang, Q.-L. Wang, X.-Y. Xu, J.-Z. Li, L.-B. Gao, W.-K. Kang, J.-S. Shi and J. Wang, *J. Mater. Chem. C*, 2013, **1**, 8033–8040.
55 G. Zhu, Z. Li, C. Wang, F. Zhou, Y. Shi, Y. Wen and S. Xin, *J. Mater. Sci.: Mater. Electron.*, 2018, **29**, 2216–2221.
56 M. Fuwang, C. Peican, G. Anxiang, W. ZHANG and Z. Liya, *J. Rare Earths*, 2015, **33**, 1064–1071.
57 Q. Sun, S. Wang, B. Li, H. Guo and X. Huang, *J. Lumin.*, 2018, **203**, 371–375.
58 A. G. Bispo, D. A. Ceccato, S. A. Lima and A. M. Pires, *RSC Adv.*, 2017, **7**, 53752–53762.
59 C. Feldmann, T. Jüstel, C. Ronda and D. Wiechert, *J. Lumin.*, 2001, **92**, 245–254.
60 X. Zhao, J. Wang, L. Fan, Y. Ding, Z. Li, T. Yu and Z. Zou, *Dalton Trans.*, 2013, **42**, 13502–13508.
61 A. R. Sharits, J. F. Khoury and P. M. Woodward, *Inorg. Chem.*, 2016, **55**, 12383–12390.
62 J. Chen, Y. Liu, L. Mei, P. Peng, Q. Cheng and H. Liu, *Sci. Rep.*, 2016, **6**, 31199.
63 S. H. Lee, Y. Cha, H. Kim, S. Lee and J. S. Yu, *RSC Adv.*, 2018, **8**, 11207–11215.
64 X. Min, Y. Sun, L. Kong, M. Guan, M. Fang, Y. g. Liu, X. Wu and Z. Huang, *Dyes Pigm.*, 2018, **157**, 47–54.
65 J. He, Z. Gao, S. Liu, J. H. Jeong, R. Yu and B. Deng, *J. Lumin.*, 2018, **202**, 7–12.